Journal of Materials Chemistry A

COMMUNICATION

View Article Online
View Journal | View Issue

Cite this: J. Mater. Chem. A, 2017, 5, 5273

Received 10th January 2017
Accepted 23rd February 2017

DOI: 10.1039/c7ta00314e

rsc.li/materials-a

Nanofiber networks of $Na_3V_2(PO_4)_3$ as a cathode material for high performance all-solid-state sodium-ion batteries†

Rongtan Gao,‡ Rui Tan,‡ Lei Han, Yan Zhao, Zijian Wang, Luyi Yang* and Feng Pan*

Herein, we fabricated a novel all-solid-state sodium-ion battery (SIB) using $Na_3V_2(PO_4)_3$ with a nanofiber network structure as the cathode material and a PEO solid polymer electrolyte (SPE) membrane, demonstrating a high reversible capacity and good cycling stability at high rates. Our study shows that the nanofiber morphology of cathode materials has significantly improved the battery's performance, especially with a high loading of cathode materials. Therefore, a promising route to improve all-solid-state batteries' rate performance is proposed.

Nowadays, sodium ion batteries (SIBs) have become a promising alternative to lithium ion batteries (LIBs), due to the rich natural abundance and low cost of sodium, as well as its chemical similarity to lithium.[1–6] Nevertheless, Na^+ insertion/extraction is more difficult than Li^+ insertion/extraction, owing to the larger radius of Na^+ (0.98 Å) compared to that of Li^+ (0.69 Å).[7] Thus it is essential to develop cathode materials with a large open framework and robust structure. Among various types of cathode materials for SIBs (*e.g.* sulfides, fluorides, phosphates, sulfates, fluorophosphates and layered transition-metal oxides), sodium superionic conductor (NASICON) compounds are build-ups of large polyanion frameworks which provide stable structures and larger ion transport channels.[4,8–11] They were initially explored as solid electrolytes before being investigated as electrode materials recently. As a widely studied cathode material, $Na_3V_2(PO_4)_3$ (NVP) exhibits an impressive energy density (400 W h kg^{-1}, corresponding to 118 mA h g^{-1}) and good thermal stability.[9] Nevertheless, the poor intrinsic electronic conductivity of NVP restricts its performance.[12] In order to improve its electronic conductivity, different carbon-coating methods have been proposed, such as tuning of carbon matrix dimensions, mesoporous carbon decoration and graphene coating.[13–15] In addition to carbon coating strategies, morphological modification of NVP also shows significant effects on its electrochemical performances and structural stability.[16,17]

Nevertheless, most research studies are currently focused on SIBs using traditional liquid electrolytes, which still suffer from safety problems caused by the instability of liquid electrolytes at high temperatures.[18] Therefore, all-solid-state batteries have been proposed as a solution due to their nonflammability, good thermal stability, higher power density and lower costs.[19–21] However, compared to liquid SIBs, less attention has been paid to the field of all-solid-state SIBs.[22–25]

Solid polymer electrolytes (SPEs) are commonly studied in all-solid-state batteries due their flexibility, ease of fabrication and ability of retaining contact at an electrode/electrolyte interface.[19,20,26,27] Poly(ethylene oxide) (PEO) based electrolytes have been widely investigated since being discovered by Wright and co-workers due to their low cost, nontoxicity and broader electrochemical windows.[26–28] In order to improve the ionic conductivity of PEO-based electrolytes, various types of inorganic fillers were introduced to disorder the crystallization of PEO and promote the dissociation of charge carriers (Li^+/Na^+) from their salts.[29–32]

Attempts to improve all-solid-state batteries are mostly devoted to promoting the ionic conductivity of electrolytes, while the structure of cathodes and the contact between the cathode and electrolyte are equally important.[33,34] Due to the lower mobility of solid electrolytes, the permeation of electrolytes and the electrolyte–electrode contact are not satisfactory compared with those of aprotic electrolytes. When the active material loading is increased, bulks which are far away from the electrode/electrolyte interface become isolated and inactive, resulting in poor rate performances and cycling stability. Herein, a network of nanofibers is employed as a 3D structure, because of (1) the shortened ion diffusion pathways,[35] (2) the higher surface area which improves the interfacial contact

School of Advanced Materials, Peking University, Peking University Shenzhen Graduate School, Shenzhen 518055, China. E-mail: panfeng@pkusz.edu.cn; Tel: +86-755-26033200

† Electronic supplementary information (ESI) available: Experimental procedures, X-ray diffraction of precursors, thermal stability, and electrochemical measurements. See DOI: 10.1039/c7ta00314e

‡ These authors contributed equally to this work.

between electrodes and electrolytes,[35] (3) structural stability to avoid agglomeration and (4) higher packing density compared with particle materials.

In this work, we fabricated all-solid-state sodium ion batteries using nanofiber networks of $Na_3V_2(PO_4)_3$ nanocrystals as the cathode active materials, a PEO/$NaClO_4$/Al_2O_3 membrane as the SPE and metallic sodium as the anode. By comparing the performances of $Na_3V_2(PO_4)_3$-nanofiber (NVP-F) and microparticle structured $Na_3V_2(PO_4)_3$-sphere (NVP-S), a preliminary study on the effects of active materials' morphologies on all-solid-state batteries is presented. Following the strategy, we demonstrate a novel all-solid-state SIB with a high reversible capacity of 96 mA h g^{-1} at a high current density of 2C and 87.5% capacity retention after 1000 cycles. Table S1† shows the summary of all the research work on all-solid-state SIBs in the past five years, from which it can be concluded that the reversible capacity, rate performances and cycling stability presented in this work are better than most of the previously reported ones.

The synthesis processes of NVP-F and NVP-S are described by a schematic illustration as shown in Fig. 1. The NVP was synthesized by a typical solvothermal method reported previously (details are shown in the ESI†).[16] In order to obtain micrometer scale spherical NVP-S, the solution was solvothermally treated for 15 h with a fast nucleation process, followed by the annealing procedure at 700 °C with a rapid heating rate of 10 °C min^{-1} to promote the agglomeration. For NVP-F, solvothermal time was increased to 30 h, leading to a recrystallization process to form the nanofiber network structure. Then the NVP-F precursor was preheated at 400 °C for 4 h and maintained at 700 °C for 8 h, with a slower heating rate of 3 °C min^{-1} to protect the delicate structure. The morphologies of the samples were characterized by scanning electron microscopy (SEM). Fig. 2a and b clearly display the difference between NVP-F and NVP-S, which are constituted by nanofibers and microspheres, respectively (SEM image of NVP-S with a low magnification is shown in Fig. S1†). X-ray diffraction (XRD) measurements were used to confirm the crystal structures of NVP-F and NVP-S. As shown in Fig. S2,† the precursors crystallized poorly and did not form the typical NVP phase. As observed from Fig. 2c, the diffraction patterns of the two materials after annealing are well indexed to the rhombohedral NVP structure (JCPDS no. 53-0018).[36] The diffraction peaks and intensities of both NVP-F and NVP-S can be indexed to the typical NASICON structure with the $R\bar{3}c$ space group. To further determine the crystallinity and crystal orientation in NVP-F, its detailed structure was investigated by transmission electron microscopy (TEM) and high solution transmission electron microscopy (HRTEM). The TEM image of the full view shows the well-connected network of NVP nanofibers (inset of Fig. 2d). Upon inspection of the HRTEM images, well-defined lattice fringes were observed, indicating high crystallinity within nanofibers. The lattice fringes with a *d*-spacing of 4.37 Å fit with the (110) planes of the NASICON structure NVP well (Fig. 2d). Moreover, according to Song's report, as Na^+ migrates along the [100] and [010] directions within NVP,[37] both materials form a 45° angle with the microfiber's cross-section (whose diameter ranges from 30 to 50 nm). In this case, the Na^+ insertion/extraction pathways have been greatly shortened. In order to determine the thermal stability and the carbon content of the samples, thermogravimetric analysis (TG) measurements were carried out (Fig. S3†). The results demonstrated good thermal stability of both NVP materials and the carbon contents of NVP-F and NVP-S were 9.22% and 8.80%, respectively.

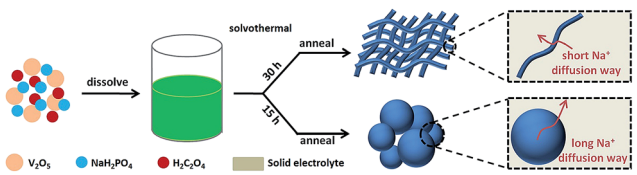

Fig. 1 Schematic illustration of the preparation of NVP-F and NVP-S.

The PEO/$NaClO_4$/Al_2O_3 membrane was prepared by a simple solution evaporation method (details are shown in the ESI†). The obtained homogeneous membrane was kept under an argon atmosphere (inset of Fig. 3a). Fig. 3a shows the smooth surface of the electrolyte membrane with well dispersed Al_2O_3 nanoparticles. Differential Scanning Calorimetry (DSC) was carried out to determine the amorphous transition temperature of the electrolyte membrane and the pristine PEO. As shown in Fig. 3b, the melting temperature (T_m) of the electrolyte membrane was significantly lowered from 71.1 °C to 64.3 °C by the addition of $NaClO_4$, and then was further decreased to 62.3 °C by the addition of inorganic filler Al_2O_3. The results indicate that $NaClO_4$ and Al_2O_3 can disorder the crystalline domain of PEO, consequently improving the segmental mobility of polymer chains. Therefore, the appropriate operating temperature of the batteries ranges from the T_m of electrolytes (62.3 °C) to the T_m of sodium (97.7 °C). The effect of molar ratios of ethylene units to Na^+ on the electrolytes' ionic conductivity at 80 °C is shown in Fig. S4.† The ionic conductivity increased as the ratio increased from 10 : 1 to 20 : 1 and started to decrease when the ratio was increased to 25 : 1, which can be explained by the balance between the better ion-dissociating ability and the decreasing charge carrier concentration. Therefore, we chose the optimized PEO_{20}/$NaClO_4$/Al_2O_3 membrane for our following experiments, as it has the highest ionic conductivity. As shown in Fig. S5,† through a gradient study of the Al_2O_3 content (1, 2, 5, 8, 10, and 15 wt%), we chose 5 wt% of Al_2O_3 as the inorganic filler for the electrolyte membrane. The Arrhenius plots of the PEO/$NaClO_4$/Al_2O_3 membrane are shown in Fig. 3c, along with the PEO membrane containing $LiClO_4$ salt. The two curves are similar in both values and variation trends, indicating that the ionic conductivity of Na^+ in PEO is similar to that of Li^+. To determine the electrochemical stability of the electrolyte membrane at high voltages, linear sweep voltammetry (LSV) measurements were conducted. As shown in Fig. 3d, no obvious decomposition can be observed until the voltage reached 4.59 V *versus* Na^+/Na, which confirmed that the membrane can adapt to the voltage window of NVP.

To evaluate the effect of NVP's morphologies on its electrochemical performance, coin-type half cells were assembled and tested. Charge–discharge curves of the all-solid-state SIBs in the first cycle, which were cycled between 2.3 and 3.9 V at 0.2C, are

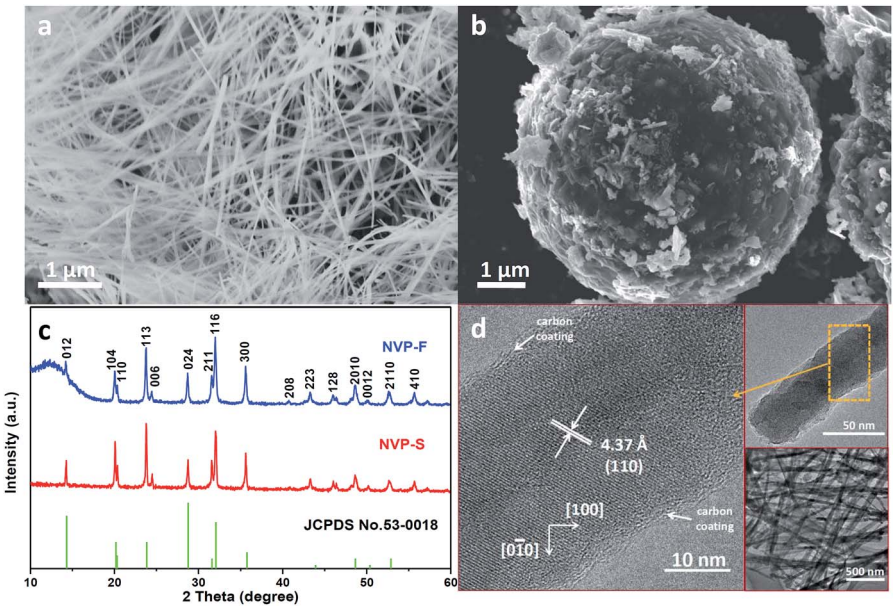

Fig. 2 SEM images of (a) NVP-F and (b) NVP-S, (c) XRD patterns of the NVP-F and NVP-S. (d) TEM (up and bottom right) and HRTEM (left) images of NVP-F.

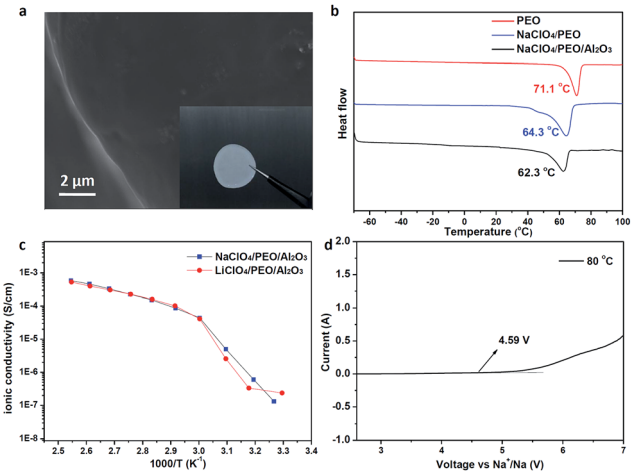

Fig. 3 Basic characterisations of the as-prepared $NaClO_4/PEO/Al_2O_3$ electrolyte membrane: (a) SEM image and photo (inset), (b) DSC curves compared with those of the pristine PEO and $NaClO_4$/PEO membrane, (c) Arrhenius plots of the ionic conductivity compared with that of the $LiClO_4/PEO/Al_2O_3$ membrane, and (d) linear scanning voltammogram at 80 °C.

shown in Fig. 4a. The charge and discharge plateaus were around 3.4 V and 3.3 V, respectively, corresponding to the reversible transformation of V^{3+}/V^{4+}. The NVP-F delivered a lower overpotential (45 mV) and higher capacity (107.5 mA h g^{-1}) compared to those of NVP-S (70 mV and 101.5 mA h g^{-1}). The inset of Fig. 4a shows that when the C-rate was increased to 2C, the overpotential of NVP-F increased to 90 mV and the capacity remained at 96.8 mA h g^{-1}; while the overpotential of NVP-S sharply increased to 170 mV and the capacity was only 59.6 mA h g^{-1}. The corresponding redox couple properties were also demonstrated by cyclic voltammetry (CV) at a scan rate of 0.1 mV s^{-1}, as shown in Fig. S6.† It can be seen from the cyclic voltammograms that NVP-F shows a larger peak area compared with that of the NVP-S, which corresponds to its higher specific capacity. The smaller peak-to-peak separation and higher redox peak specific current indicated the lower polarization and the faster kinetics for Na^+ insertion/extraction. To further understand the effect of morphological modification, electrochemical impedance spectroscopy (EIS) was performed (Fig. 4b). In the Nyquist plots, the impedance spectra of the as-prepared NVP-F all-solid-state cell is comprised of two semicircles and one inclined line, corresponding to the electrolyte resistance (R_e), charge transfer resistance (R_{ct}) and the Warburg impedance respectively. The R_{ct} of the NVP-F cell (390 Ω) is much lower than that of NVP-S cell (630 Ω), demonstrating that the improved rate performances can be attributed to the better interfacial contact between PEO and the nanofiber network of NVP. The specific surface areas of NVP-F and NVP-S are 80.7 and 53.6 m^2 g^{-1}, which further support the claim that the NVP-F has better contact with the electrolyte (the nitrogen adsorption–desorption isotherms are shown in Fig. S7†). The rate performances of NVP-F and NVP-S from 0.2C to 2C are shown in Fig. 4c. The reversible capacity of 108, 105, 102 and 97 mA h g^{-1} was obtained for NVP-F at the C-rates of 0.2, 0.5, 1 and 2C, respectively; while those of NVP-S were 104, 99, 87 and 60 mA h g^{-1}. When the current density was reverted to 0.2C again, the reversible capacity of 108 mA h g^{-1} can be recovered for the NVP-F electrode, exhibiting great reversibility and stability. The better rate performance delivered by NVP-F can be attributed to two features of its nanofiber network structure discussed above: (1) the shortened Na^+ diffusion pathways; (2) the better electrode/electrolyte contact. In addition, a contrast experiment of cycling SIBs using a liquid electrolyte at the same series of rates is shown in Fig. S8.† Different from the case of all-solid-state batteries, the rate performances of the two samples are similar, indicating the remarkable effect of

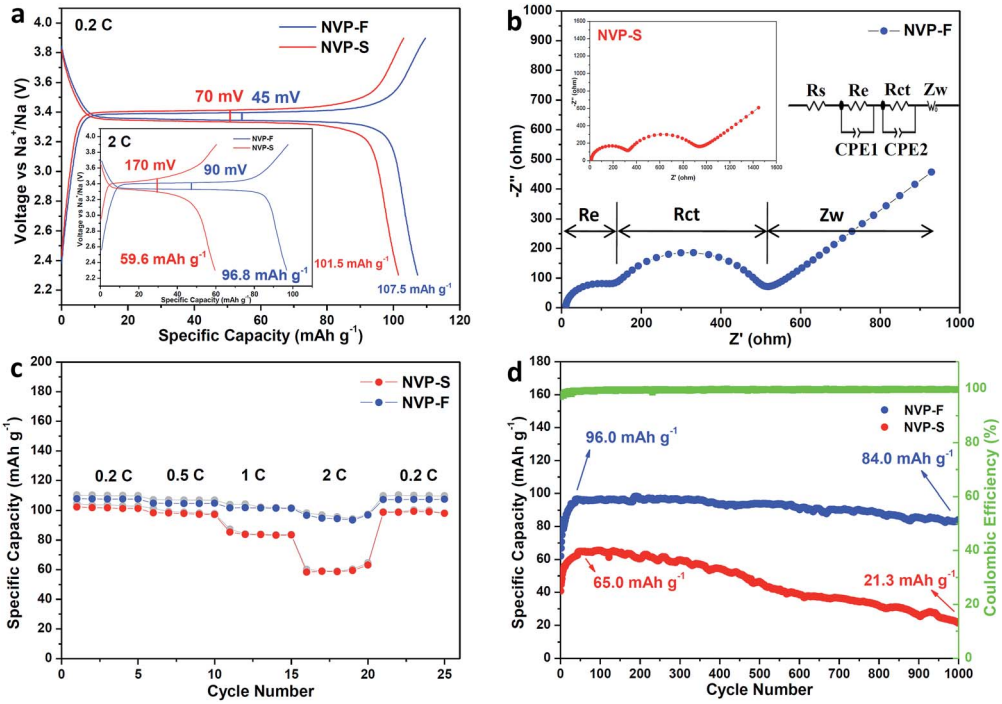

Fig. 4 Electrochemical characterisation of the as-prepared NVP all-solid-state cells: (a) charge–discharge curves of NVP-F and NVP-S at the C-rates of 0.2C and 2C (inset), (b) EIS plots of NVP-F and the equivalent circuit diagram (inset shows the EIS plots of NVP-S), (c) rate performances of NVP-F and NVP-S, and (d) long-term cycling performances of NVP-F and NVP-S at the C-rate of 2C. All measurements were carried out at 80 °C.

the morphology on all-solid-state batteries. The long-term cycling performances of NVP-F and NVP-S at the rate of 2C are shown in Fig. 4d. After an activation process for a few cycles, NVP-F delivered a reversible capacity as high as 96.0 mA h g^{-1} and the capacity was retained at 84.0 mA h g^{-1} after 1000 cycles, corresponding to a capacity retention of 87.5% and a capacity decay of 0.0125% per cycle, with almost 100% coulombic efficiency (except for the first few cycles). By contrast, the NVP-S delivered an initial reversible capacity of 65.0 mA h g^{-1} and the remaining capacity after 1000 cycles was only 21.3 mA h g^{-1} (32.8%). This result may be an indication that the nanofiber network provides better stability to the cathode. The corresponding charge–discharge curves are shown in Fig. S9,† from which the increased polarization of NVP-F can be observed. Besides, the capacity increased during the electrochemical activation process at first and decayed thereafter. Furthermore, since a high active material loading is desirable in all batteries, all-solid-state SIBs with thicker cathodes were assembled and tested. As shown in Fig. S10,† when the active material loading was increased from 0.7–1.0 to 2.2–2.7 mg cm^{-2}, the cell using NVP-S as the active material showed a rapid decrease in the capacity in the 100th cycle from 63.1 mA h g^{-1} (53.5% of the theoretical capacity) to merely 30.1 mA h g^{-1} (25.5% of the theoretical capacity). In comparison, when the same loading of NVP-F was used, there was no significant decrease in the capacity (from 95.2 to 91.9 mA h g^{-1}). Therefore, it can be concluded that with a thicker cathode, the electrode/electrolyte contact becomes more crucial. Because the NVP cathode with a nanofiber network structure provides shorter Na^+ diffusion pathways and better electrode/electrolyte contact, superior cycling performance can be expected with a high loading of materials.

Conclusions

In summary, a novel all-solid-state SIB has been demonstrated by using nanofiber networks of $Na_3V_2(PO_4)_3$ nanocrystals as the cathode material and a PEO/$NaClO_4$/Al_2O_3 membrane as the electrolyte. The battery shows not only a high reversible capacity (107 mA h g^{-1} at 0.2C and 96 mA h g^{-1} at 2C), but also a good cycling stability (87.5% capacity retained after 1000 cycles at 2C), which is remarkable in the field of all-solid-state SIBs. Moreover, we further demonstrate the advantages of the nanofiber network structure of NVP under high-loading conditions of cathode materials. The improved performances lead us to expect that morphological modification of cathode materials can be an effective approach to develop all-solid-state SIBs.

Acknowledgements

This work was financially supported by the National Materials Genome Project (2016YFB0700600), National Science Foundation of China (51602009), Guangdong Innovation Team Project (2013N080) and Shenzhen Science and Technology Research Grant (JCYJ20140903101633318, Peacock Plan KYPT20141016105435850 and JCYJ20160531141048950).

Notes and references

1 B. Zhang, R. Dugas, G. Rousse, P. Rozier, A. M. Abakumov and J.-M. Tarascon, *Nat. Commun.*, 2016, **7**, 10308.
2 L. Wang, Y. Lu, J. Liu, M. Xu, J. Cheng, D. Zhang and J. B. Goodenough, *Angew. Chem.*, 2013, **125**, 2018–2021.

3 Y. Sun, L. Zhao, H. Pan, X. Lu, L. Gu, Y.-S. Hu, H. Li, M. Armand, Y. Ikuhara, L. Chen and X. Huang, *Nat. Commun.*, 2013, **4**, 1870.
4 M. D. Slater, D. Kim, E. Lee and C. S. Johnson, *Adv. Funct. Mater.*, 2013, **23**, 947–958.
5 J. Lu, Z. Chen, Z. Ma, F. Pan, L. A. Curtiss and K. Amine, *Nat. Nanotechnol.*, 2016, **11**, 1031–1038.
6 J. Zheng, T. Liu, Z. Hu, Y. Wei, X. Song, Y. Ren, W. Wang, M. Rao, Y. Lin, Z. Chen, J. Lu, C. Wang, K. Amine and F. Pan, *J. Am. Chem. Soc.*, 2016, **138**, 13326–13334.
7 S. P. Ong, V. L. Chevrier, G. Hautier, A. Jain, C. Moore, S. Kim, X. Ma and G. Ceder, *Energy Environ. Sci.*, 2011, **4**, 3680–3688.
8 Y. U. Park, D. H. Seo, H. Kim, J. Kim, S. Lee, B. Kim and K. Kang, *Adv. Funct. Mater.*, 2014, **24**, 4603–4614.
9 D. Kundu, E. Talaie, V. Duffort and L. F. Nazar, *Angew. Chem., Int. Ed. Engl.*, 2015, **54**, 3431–3448.
10 J. Kim, I. Park, H. Kim, K. Y. Park, Y. U. Park and K. Kang, *Adv. Energy Mater.*, 2016, **6**, 6–9.
11 H. Su, S. Jaffer and H. Yu, *Energy Storage Materials*, 2016, **5**, 116–131.
12 J. Kang, S. Baek, V. Mathew, J. Gim, J. Song, H. Park, E. Chae, A. K. Rai and J. Kim, *J. Mater. Chem.*, 2012, **22**, 20857–20860.
13 S. Li, Y. Dong, L. Xu, X. Xu, L. He and L. Mai, *Adv. Mater.*, 2014, **26**, 3545–3553.
14 Y. Jiang, Z. Yang, W. Li, L. Zeng, F. Pan, M. Wang, X. Wei, G. Hu, L. Gu and Y. Yu, *Adv. Energy Mater.*, 2015, **5**, 1402104.
15 Y. Xu, Q. Wei, C. Xu, Q. Li, Q. An, P. Zhang, J. Sheng, L. Zhou and L. Mai, *Adv. Energy Mater.*, 2016, **6**, 1600389.
16 W. Ren, Z. Zheng, C. Xu, C. Niu, Q. Wei, Q. An, K. Zhao, M. Yan, M. Qin and L. Mai, *Nano Energy*, 2016, **25**, 145–153.
17 J. Liu, K. Tang, K. Song, P. A. van Aken, Y. Yu and J. Maier, *Nanoscale*, 2014, **6**, 5081–5086.
18 K. Xu, *Chem. Rev.*, 2014, **114**, 11503–11618.
19 J. F. M. Oudenhoven, L. Baggetto and P. H. L. Notten, *Adv. Energy Mater.*, 2011, **1**, 10–33.
20 E. Quartarone and P. Mustarelli, *Chem. Soc. Rev.*, 2011, **40**, 2525–2540.
21 R. Bouchet, S. Maria, R. Meziane, A. Aboulaich, L. Lienafa, J.-P. Bonnet, T. N. T. Phan, D. Bertin, D. Gigmes, D. Devaux, R. Denoyel and M. Armand, *Nat. Mater.*, 2013, **12**, 452–457.
22 C. W. Park, H. S. Ryu, K. W. Kim, J. H. Ahn, J. Y. Lee and H. J. Ahn, *J. Power Sources*, 2007, **165**, 450–454.
23 Y. L. Ni'Mah, M. Y. Cheng, J. H. Cheng, J. Rick and B. J. Hwang, *J. Power Sources*, 2015, **278**, 375–381.
24 A. Banerjee, K. H. Park, J. W. Heo, Y. J. Nam, C. K. Moon, S. M. Oh, S.-T. Hong and Y. S. Jung, *Angew. Chem.*, 2016, **128**, 9786–9790.
25 I.-H. Chu, C. S. Kompella, H. Nguyen, Z. Zhu, S. Hy, Z. Deng, Y. S. Meng and S. P. Ong, *Sci. Rep.*, 2016, 1–10.
26 C. Zhang, S. Gamble, D. Ainsworth, A. M. Z. Slawin, Y. G. Andreev and P. G. Bruce, *Nat. Mater.*, 2009, **8**, 580–584.
27 J. B. Goodenough and Y. Kim, *Chem. Mater.*, 2010, **22**, 587–603.
28 D. E. Fenton, J. M. Parker and P. V. Wright, *Polymer*, 1973, **14**, 589.
29 S. A. M. Noor, A. Ahmad, I. A. Talib and M. Y. A. Rahman, *Ionics*, 2011, **17**, 451–456.
30 M. R. Johan, O. H. Shy, S. Ibrahim, S. M. Mohd Yassin and T. Y. Hui, *Solid State Ionics*, 2011, **196**, 41–47.
31 R. Tan, J. Yang, J. Zheng, K. Wang, L. Lin, S. Ji, J. Liu and F. Pan, *Nano Energy*, 2015, **16**, 112–121.
32 R. Tan, R. Gao, Y. Zhao, M. Zhang, J. Xu, J. Yang and F. Pan, *ACS Appl. Mater. Interfaces*, 2016, **8**, 31273–31280.
33 Y. Kato, S. Hori, T. Saito, K. Suzuki, M. Hirayama, A. Mitsui, M. Yonemura, H. Iba and R. Kanno, *Nature Energy*, 2016, **1**, 16030.
34 X. Han, Y. Gong, K. (Kelvin) Fu, X. He, G. T. Hitz, J. Dai, A. Pearse, B. Liu, H. Wang, G. Rubloff, Y. Mo, V. Thangadurai, E. D. Wachsman and L. Hu, *Nat. Mater.*, 2016, **1**, 1–9.
35 L. Mai, X. Tian, X. Xu, L. Chang and L. Xu, *Chem. Rev.*, 2014, **114**, 11828–11862.
36 K. Saravanan, C. W. Mason, A. Rudola, K. H. Wong and P. Balaya, *Adv. Energy Mater.*, 2013, **3**, 444–450.
37 W. Song, X. Ji, Z. Wu, Y. Zhu, Y. Yang, J. Chen, M. Jing, F. Li and C. E. Banks, *J. Mater. Chem. A*, 2014, **2**, 5358.